Supplementary Information (SI) for Nanoscale.

An investigation into catalysed xanthene-based dye oxidation by a family of coordination cages

James R. Williams, Michael D. Ward*

Supporting information

S1 – Synthesis / characterisation of metal complexes

General information

All chemicals were used as supplied without further purification.

NMR spectra were recorded on Bruker Avance (300 MHz), Bruker Avance III HD (400 MHz), Bruker Avance III HD (500 MHz) spectrometers at 25°C in the indicated deuterated solvents unless stated otherwise. Low resolution ESI mass spectrometry was performed using an Agilent 6130B ESI-MS instrument; high resolution ESI mass spectra were acquired on a Bruker Compact ESI-Q-TOF instrument. UV/Vis spectra were recorded on an Implen C40 Nanophotometer and/or a Clariostar Plus (BMG Labtech) plate reader. Compounds that have been previously reported are referenced in the main text.

Complex syntheses

*Preparation of cubic cage $[Fe_8(L^A)_{12}](BF_4)_{16}$ (**Fe_8**)*

This follows the method used to prepare **Co_8** (main text, ref. 2c). $Fe(BF_4)_2 \cdot xH_2O$ (0.1 mmol) and L^A (66.3 mg, 1.5 mmol; see Fig. 1) were combined with methanol (6 cm^3) in a Teflon-lined autoclave. The suspension was heated to 120 °C at a rate of 5 °C min^{-1}, held at that temperature for 6 hours, then cooled at a rate of 0.1 °Cmin^{-1} to 105, 90, 75, 60, 45, 30 and 25 °C, holding at each temperature for 3 hours. This afforded good yields of crystals which were washed several times with methanol and dried under reduced pressure. Yield of **Fe_8**: 74.9 mg, 0.0105 mmol, 84%.

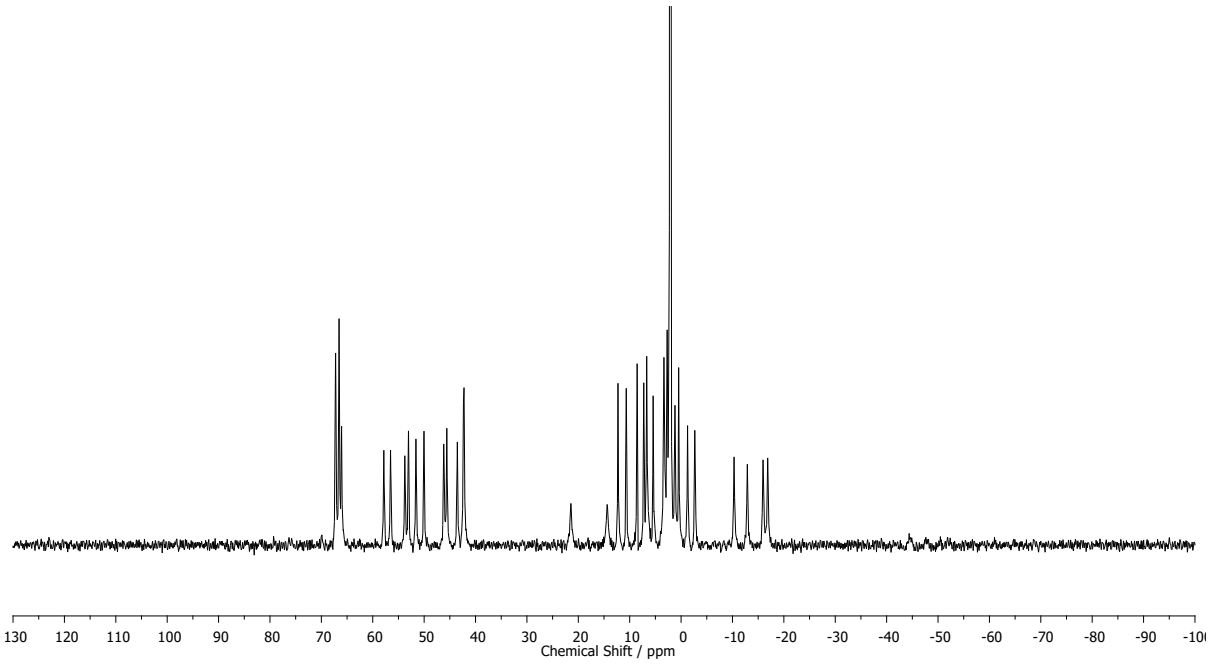

Fig. S1: ^1H NMR spectrum (300 MHz) of **Fe_8** in CD_3CN at 298 K.

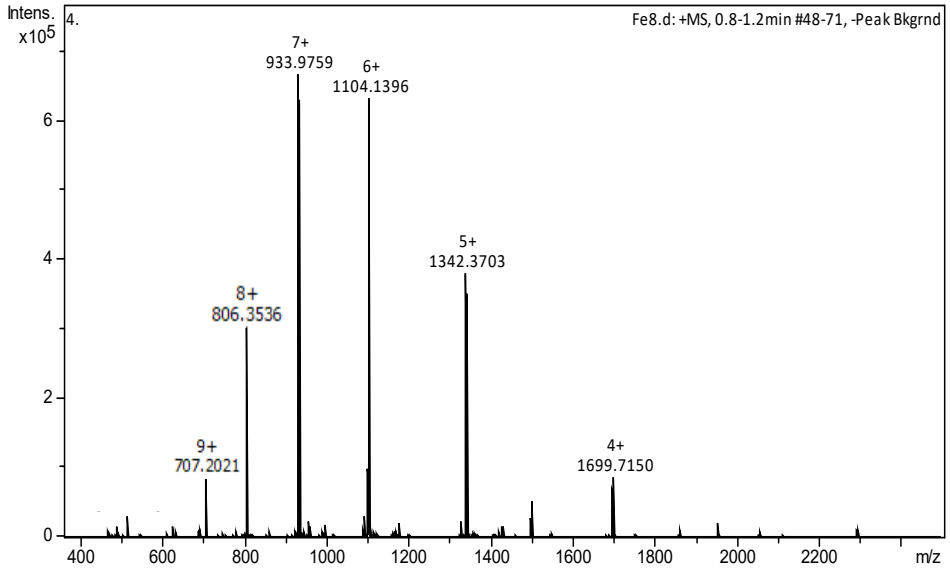

Fig. S2: HR-ESI-MS of **Fe_8** in MeCN showing {**Fe_8** – $n(BF_4^-)$}$^{n+}$ (n = 4 – 9) signals associated with sequential loss of anions.

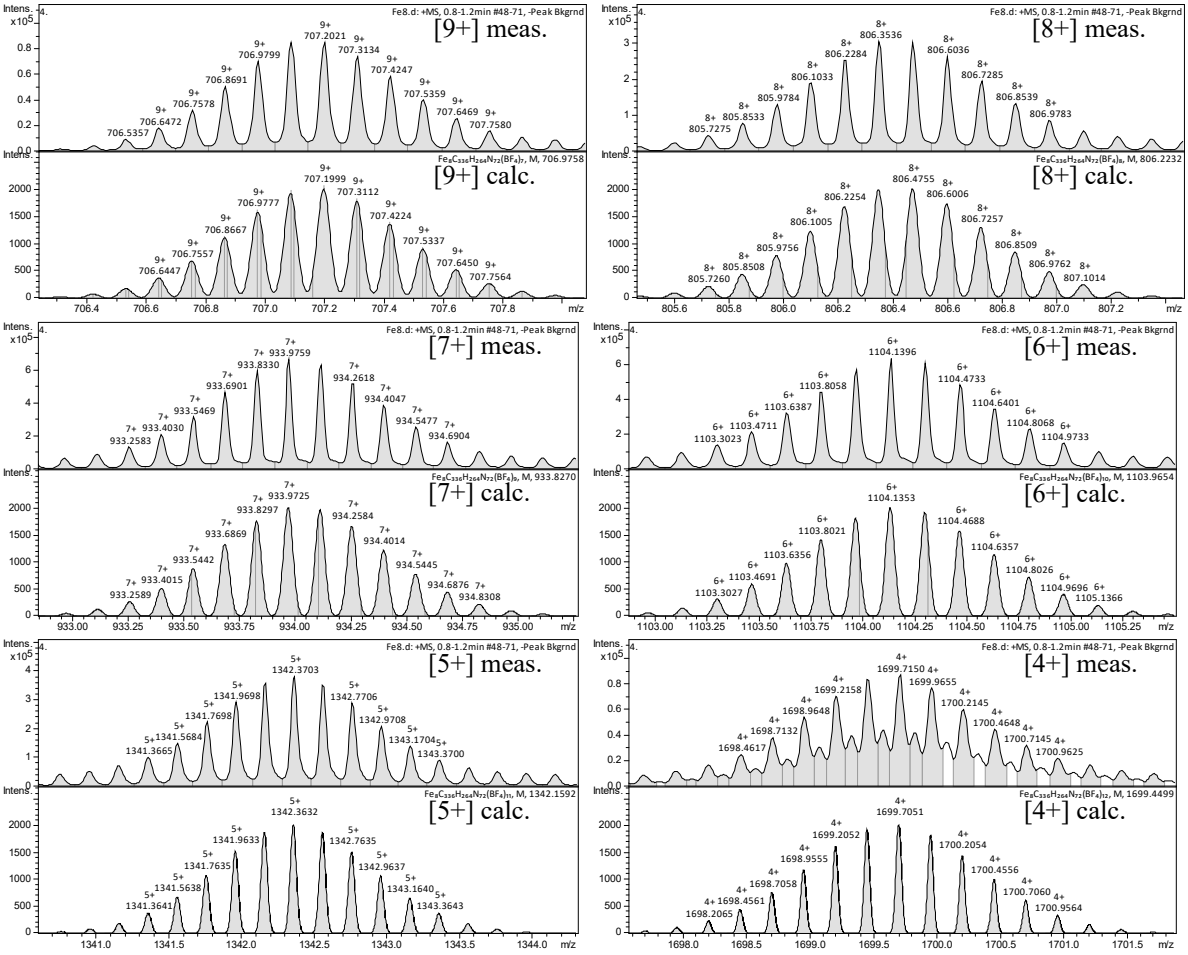

Fig. S3: HR-ESI-MS of **Fe_8** in MeCN showing expansion of signals for {**Fe_8** – $n(BF_4^-)$}$^{n+}$ (n = 4 – 10) combined with the calculated isotope patterns for each signal.

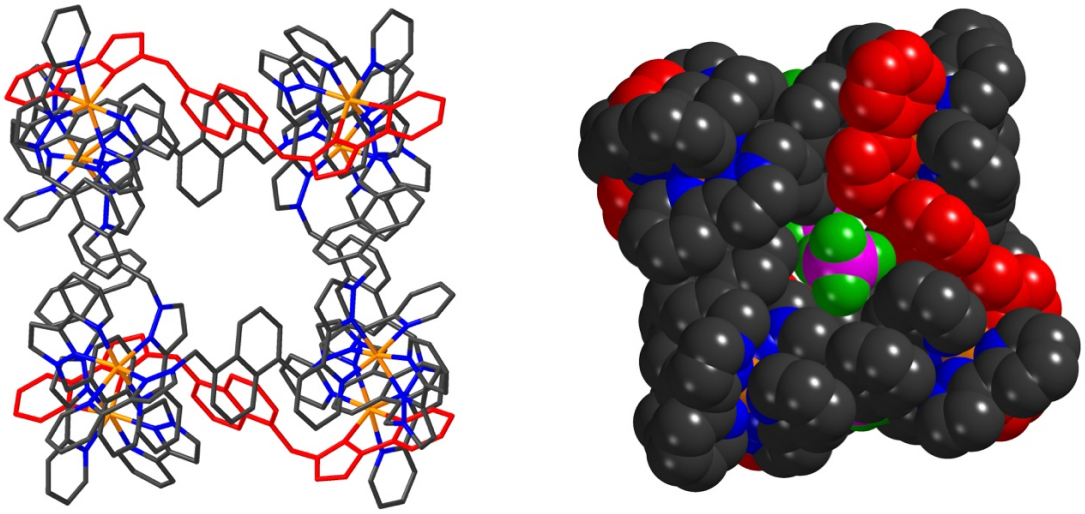

Fig. S4: Molecular structure of the complex cation of the octanuclear cage **Fe_8** from crystallographic data. Left: a wireframe view of the complex cation with two crystallographically equivalent ligands highlighted in red for clarity (the cage is centrosymmetric). Right: a space-filling view showing binding of fluoroborate anions (B – purple, F – green) in the cage windows. Fe–N distances all lie in the range 2.17 – 2.25 Å. Fe•••Fe distances between the cage vertices all lie in the range 11.16 – 11.53 Å.

*Preparation of $[M(PyPzMe)_3](BF_4)_2$ (**Co_1, Fe_1, Zn_1, Ni_1**)*

A mixture of the relevant $M(BF_4)_2 \cdot xH_2O$ (0.5 mmol) and PyPzMe (238.6 mg, 1.5 mmol) in ethanol (30 cm^3) was heated to reflux for 2 hours. The reaction mixture was then cooled to room temperature and a precipitate formed. The precipitate was collected by filtration and purified by recrystallisation from hot ethanol (~10 cm^3). The resulting crystals were collected, washed with ice cold ethanol (~10 cm^3) and dried under reduced pressure to yield the product as: **Co_1**, orange-pink crystals, (291.1 mg, 0.410 mmol, 82%); **Fe_1**, yellow-orange crystals, (243.9 mg, 0.345 mmol, 69%); **Ni_1**, blue crystals, (269.4 mg, 0.38 mmol, 76%); **Zn_1**, colourless crystals, (303.8 mg, 0.425 mmol, 85%).

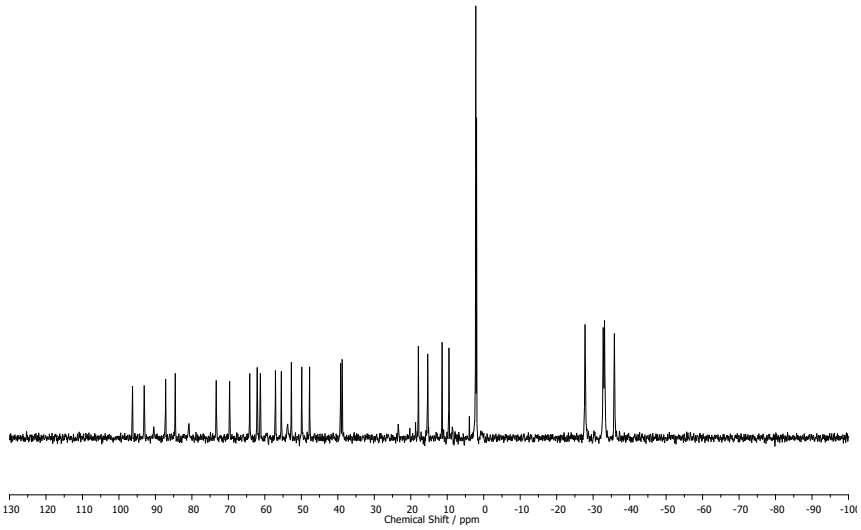

Fig. S5: ^{1}H NMR spectrum (300 MHz) of **Co_1** in CD_3CN at 298 K. The presence of signals in sets of four of equal intensity (*e.g.* 9 – 19 ppm; -28 to -38 ppm) reflects the 1:3 mixture of *fac* and *mer* isomers, see ref. 14.

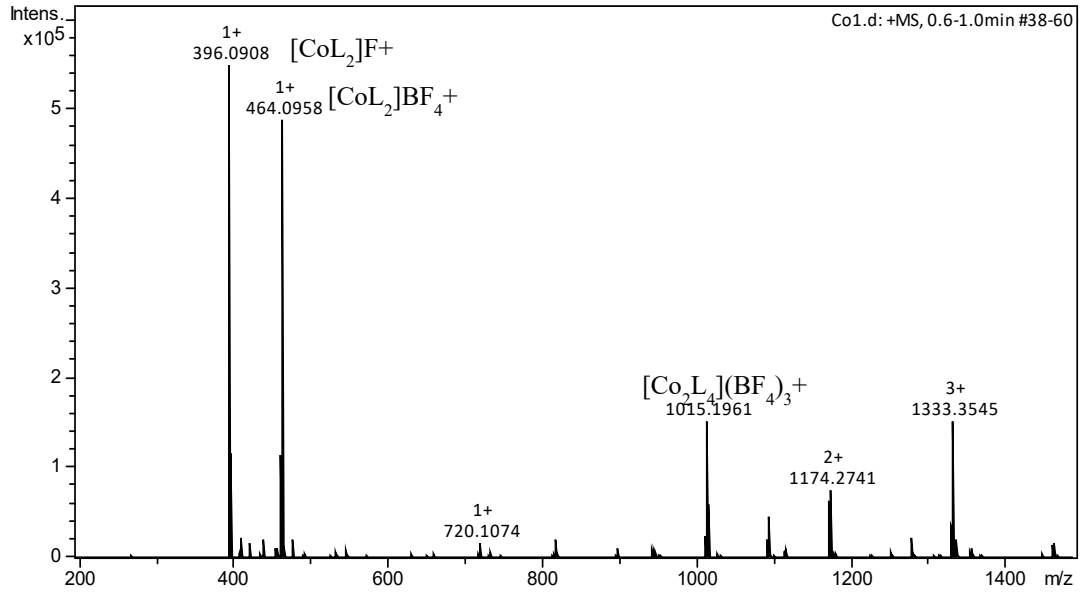

Fig. S6: HR-ESI-MS of **Co_1** in MeCN.

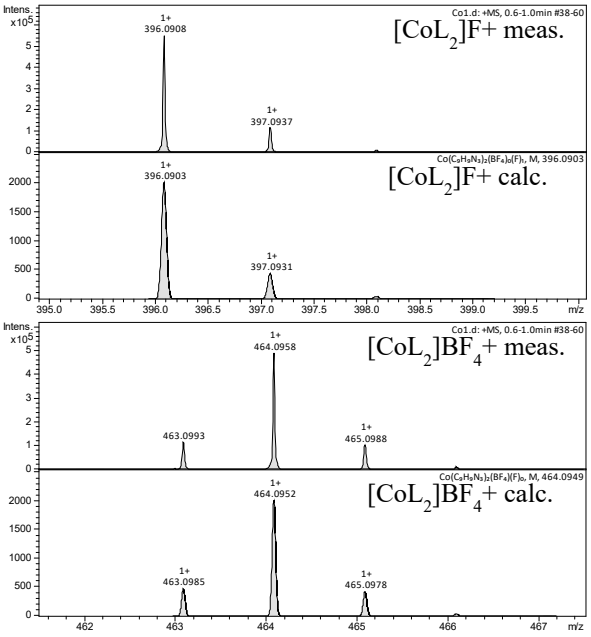

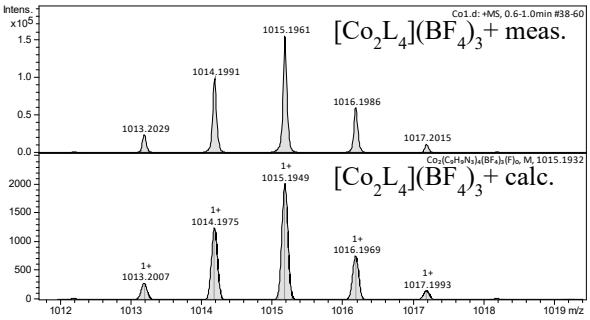

Fig. S7: HR-ESI-MS of **Co_1** in MeCN showing expansion of signals and calculated isotope patterns.

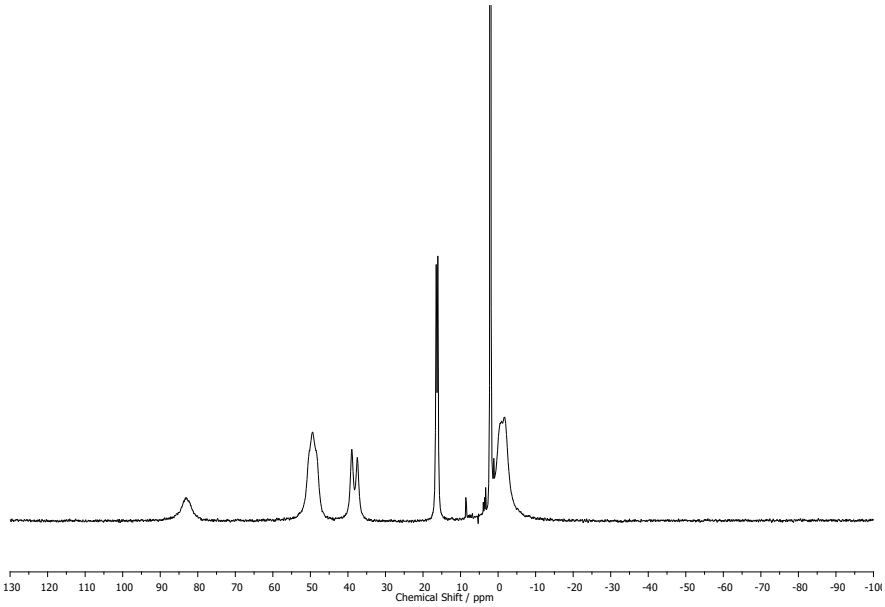

Fig. S8: ^{1}H NMR spectrum (300 MHz) of **Ni_1** in CD_3CN at 298 K.

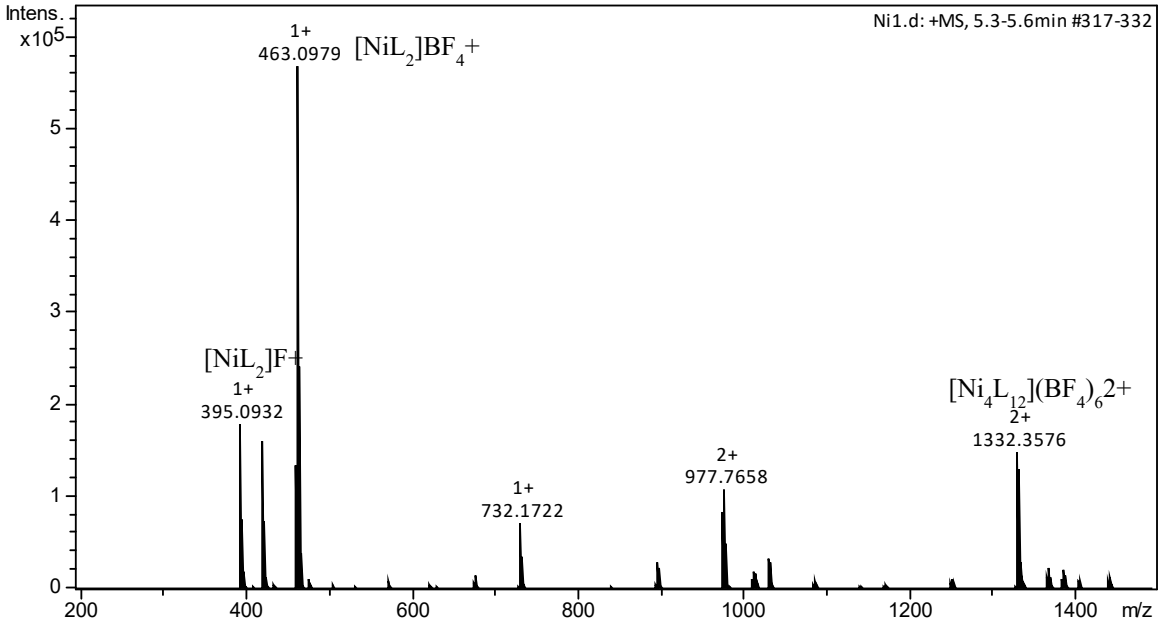

Fig. S9: HR-ESI-MS of **Ni_1** in MeCN.

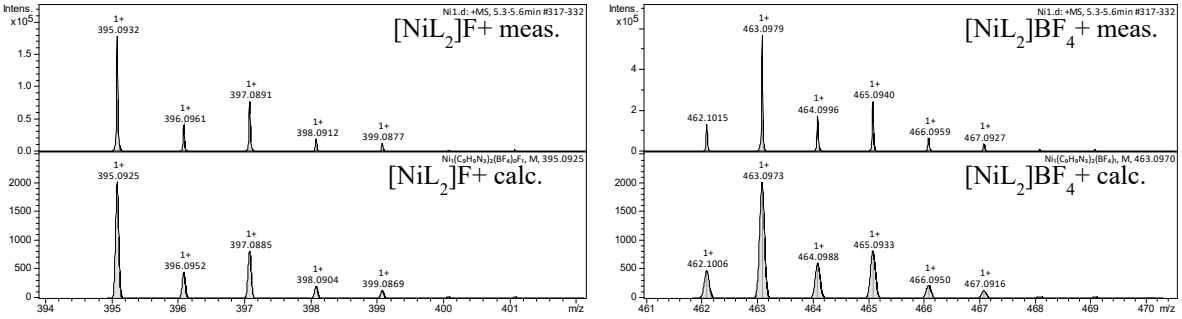

Fig. S10: HR-ESI-MS of **Ni_1** in MeCN showing expansion of signals and calculated isotope patterns.

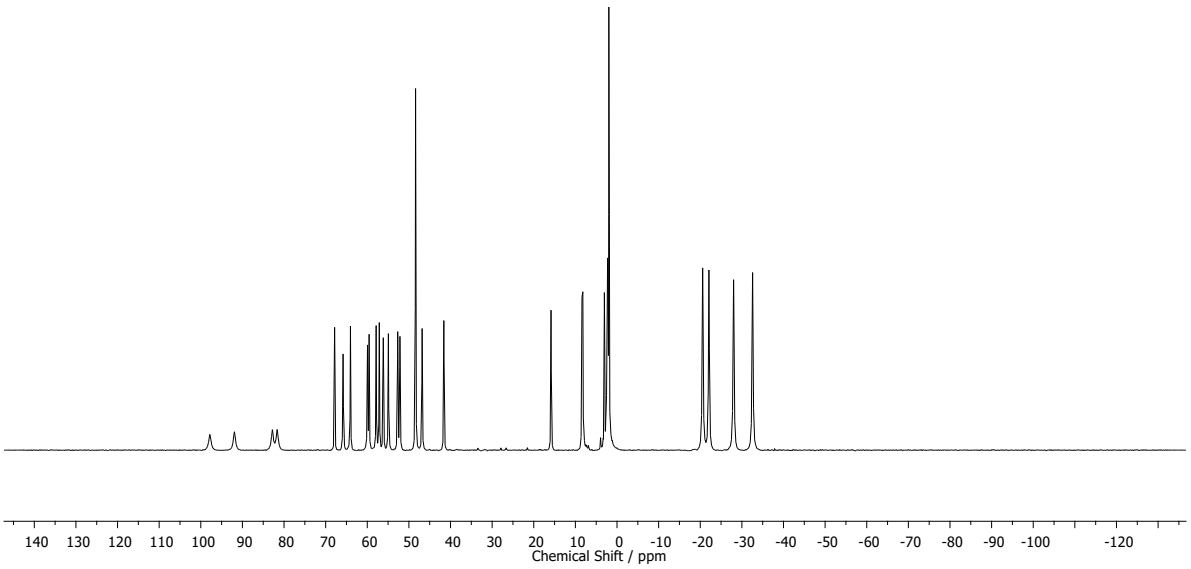

Fig. S11: ^{1}H NMR spectrum (300 MHz) of **Fe$_1$** in CD_3CN at 298 K: the presence of signals in sets of four of equal intensity (*e.g.* 80-100 ppm; -20 to -35 ppm) reflects the 1:3 mixture of *fac* and *mer* isomers, see ref. 14.

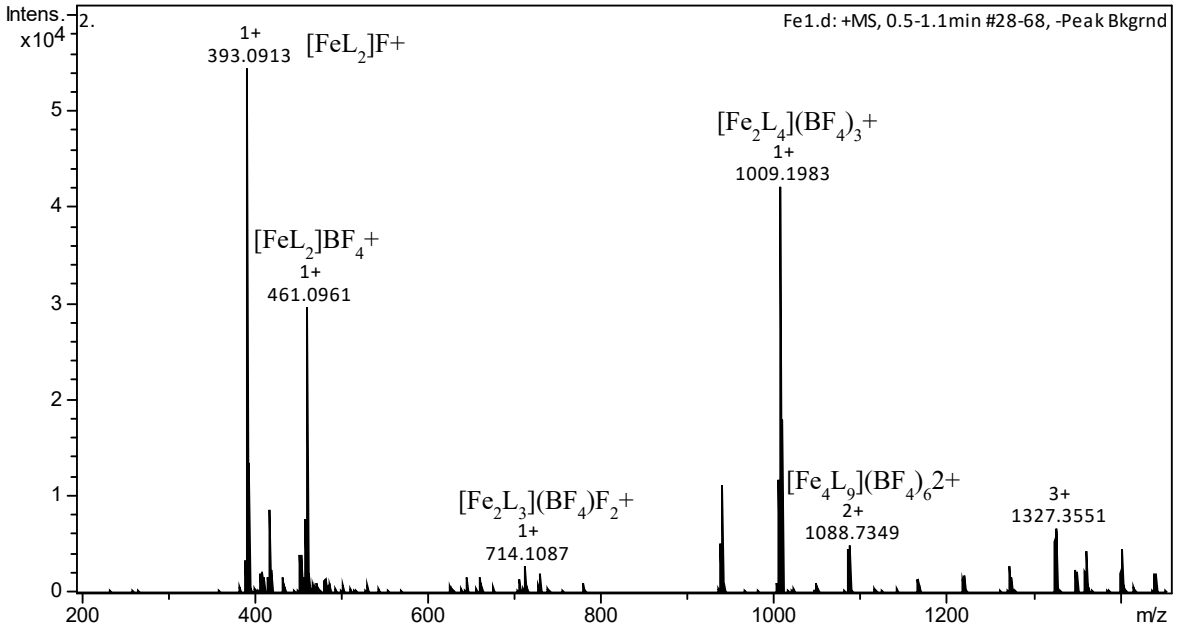

Fig. S12: HR-ESI-MS of **Fe$_1$** in MeCN.

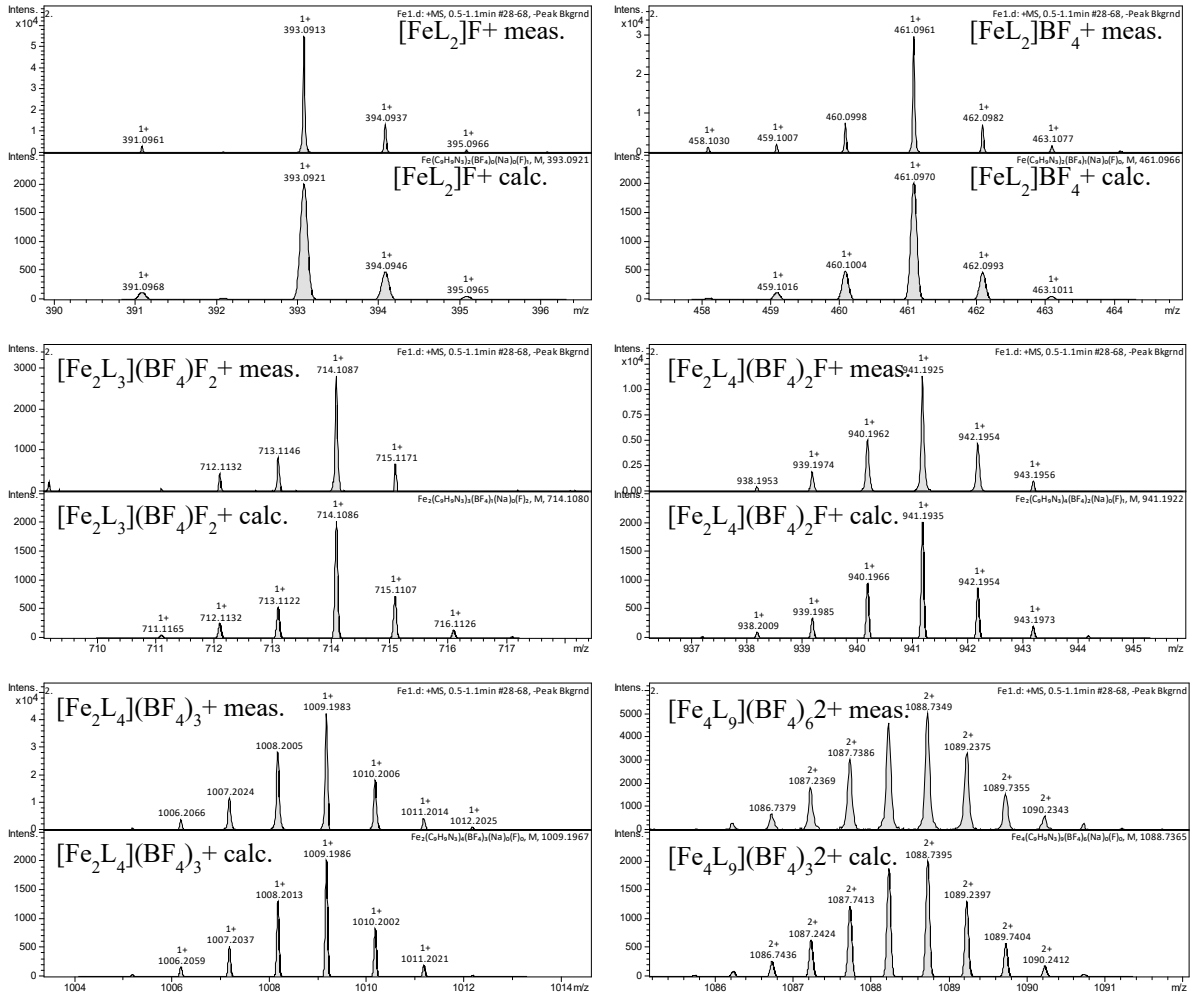

Fig. S13: HR-ESI-MS of **Fe_1** in MeCN showing expansion of signals and calculated isotope patterns.

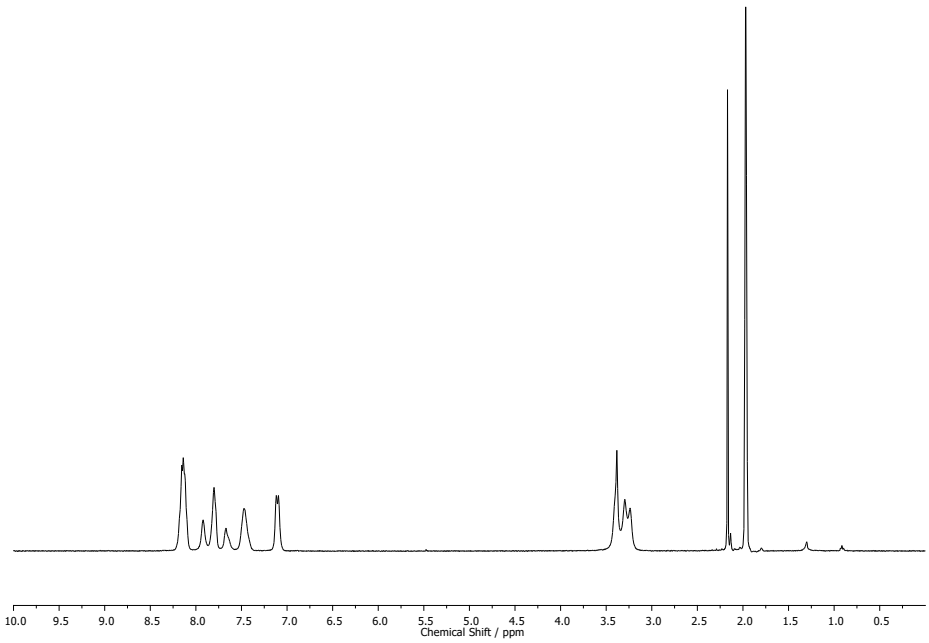

Fig. S14: ^{1}H NMR spectrum of **Zn_1** in CD_3CN at 298 K.

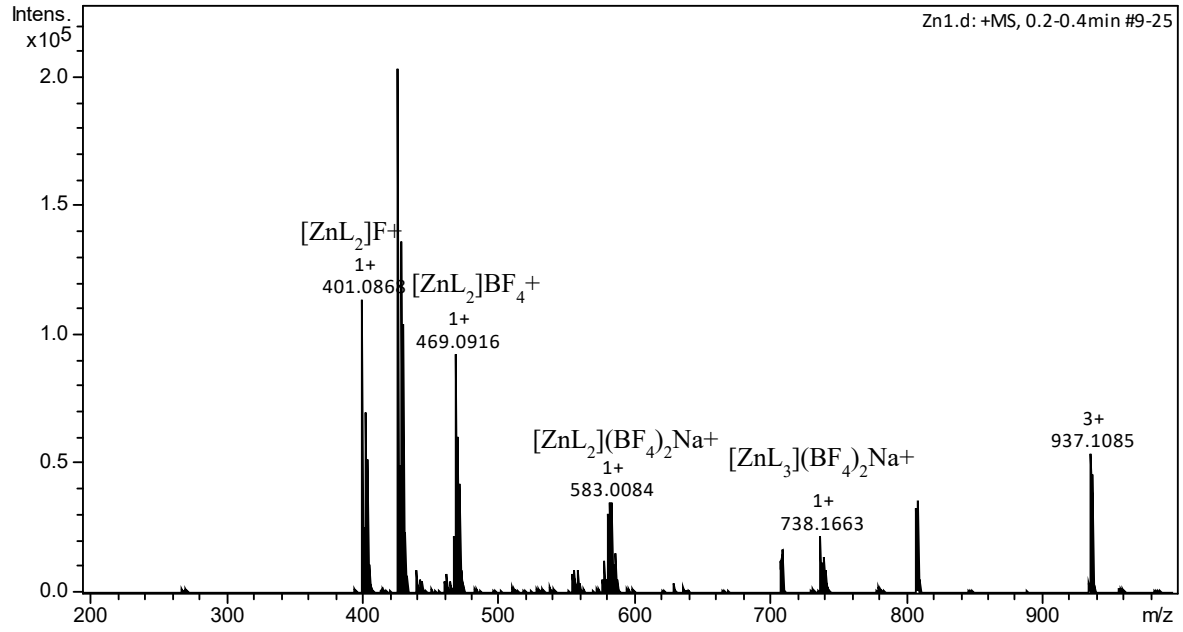

Fig. S15: HR-ESI-MS of **Zn_1** in MeCN.

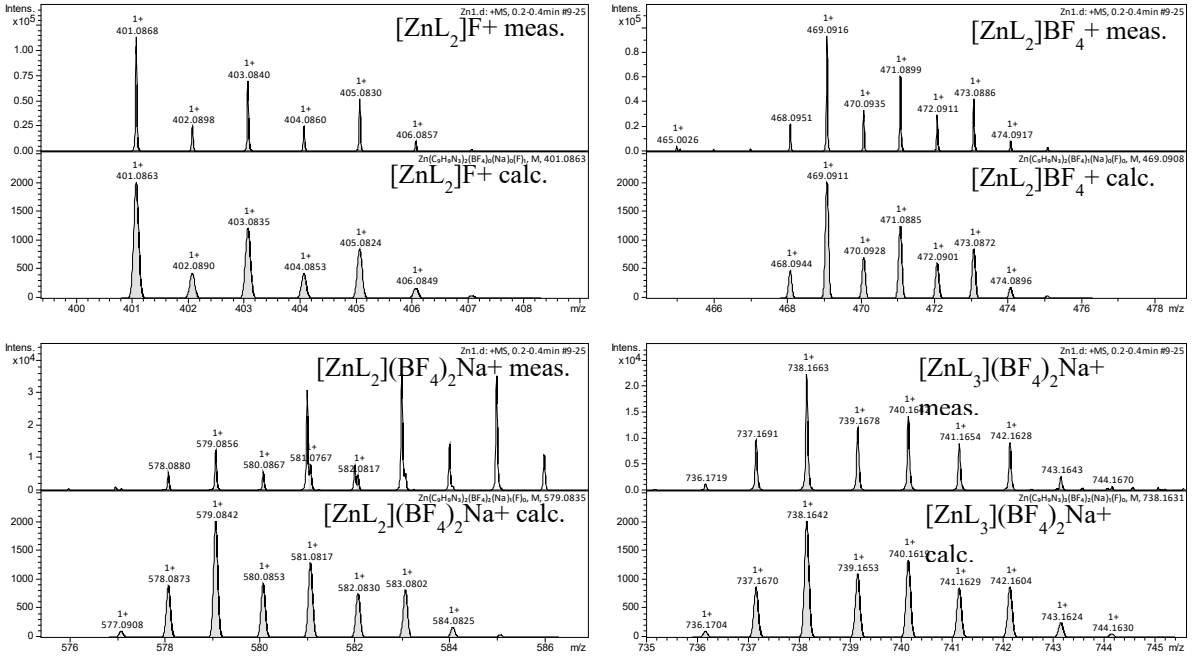

Fig. S16: HR-ESI-MS of **Zn_1** in MeCN showing expansion of signals and calculated isotope patterns.

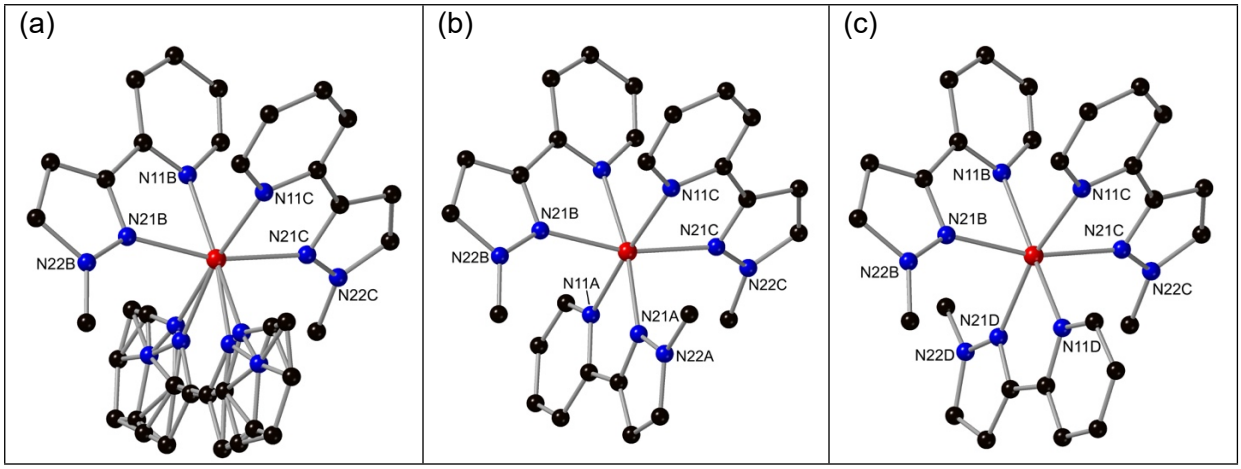

Fig. S17: Molecular structure of the complex cation of *mer*-**Co$_1$** from crystallographic data. Pane (a) shows how one ligand is disordered over two sites in the crystal structure; panes (b) and (c) show the separate components, both of which have a *mer* tris-chelate geometry. Bond distances (Å) from Co(1): N(11A), 2.117; N(21A), 2.119(8); N(11B), 2.202(4); N(21B), 2.122(4); N(11C), 2.146(4); N(21C), 2.127(4); N(11D), 2.135(18); N(21D), 2.145(17).

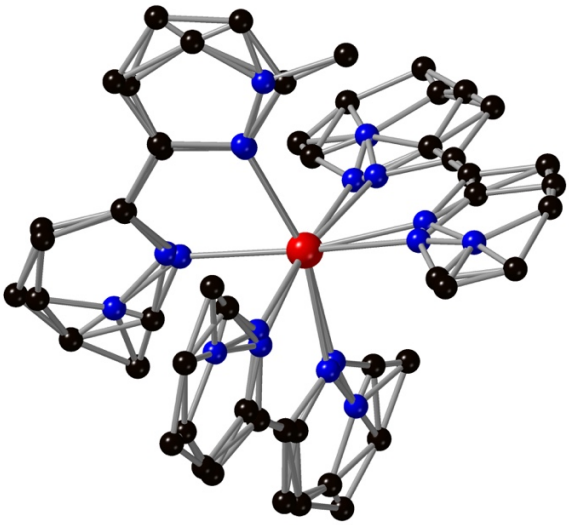

Fig. S18: Molecular structure of the complex cation of **Zn$_1$** from crystallographic data. The unit cell is isostructural with that of **Co$_1$** but all three pypz-Me ligands are disordered over two orientations, as is the Zn(II) ion, such that a superimposed mixture of *fac* and *mer* isomers is present. This dataset has not been deposited in the CCDC; the figure is included just to illustrate that the **Zn$_1$** complex has the expected mononuclear structure and is isostructural with **Co$_1$.**

S2 – Dye Binding studies

Fluorescence titrations between ***Co$_8$*** *and each dye to evaluate association of each fluorescent dye type with* ***Co$_8$***.

Solutions of dye (see Fig. 2, main text) and **Co$_8$** in 2% DMSO:Phosphate buffer (0.1 M, pH 7.0) were combined in a 96-well plate to achieve a total volume of 200 µL such that each well contained a different concentration of dye and **Co$_8$**. Absorption and fluorescence spectra were recorded on a BMG Clariostar plate reader. Fluorescence measurements used excitation at the wavelength corresponding to A = 0.1 and an emission window of appropriate width. The instrument was warmed to 25˚C, and the plate was pre-shaken to remove bubbles and allowed to equilibrate for 30 minutes before recording spectra. Plotting the degree of fluorescence quenching of the dye against dye mole fraction (Job plot) allowed binding ratio of the dyes and **Co$_8$** to be quantified. Bindfit (main text, ref. 17) was used to fit 1:1 binding isotherms to absorption and fluorescence titration data to determine an association constant for each dye with **Co$_8$**. Each titration was repeated in triplicate. Illustrative data for titrations with **FLU** and **SRB** are shown below.

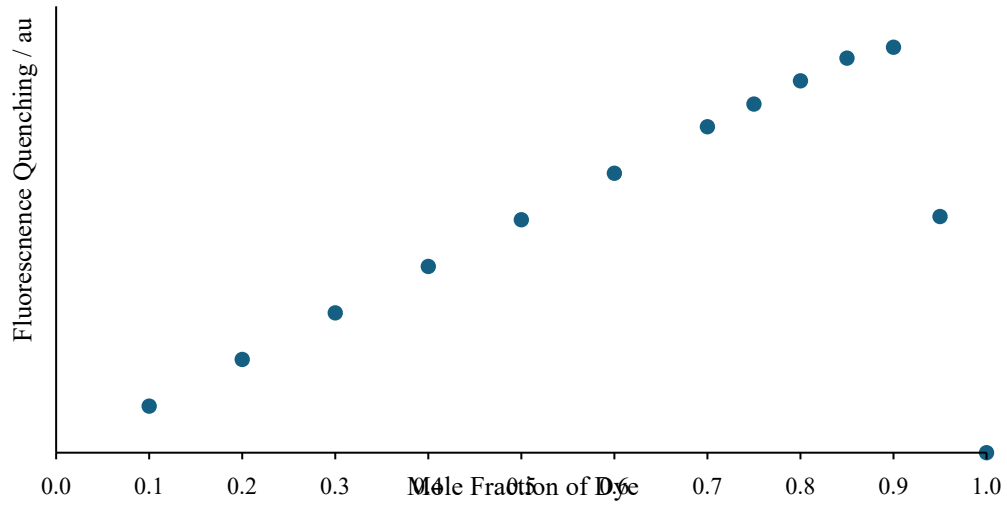

Fig. S19: Job plot showing degree of fluorescence quenching of **SRB** for varying **Co$_8$**/**SRB** mole fractions at a total combined concentration of 10 µM in phosphate buffer (0.1 M pH 7.0), indicating a high degree of association of **SRB** with the cage in solution (*ca.* 8:1 SRB:**Co$_8$** binding).

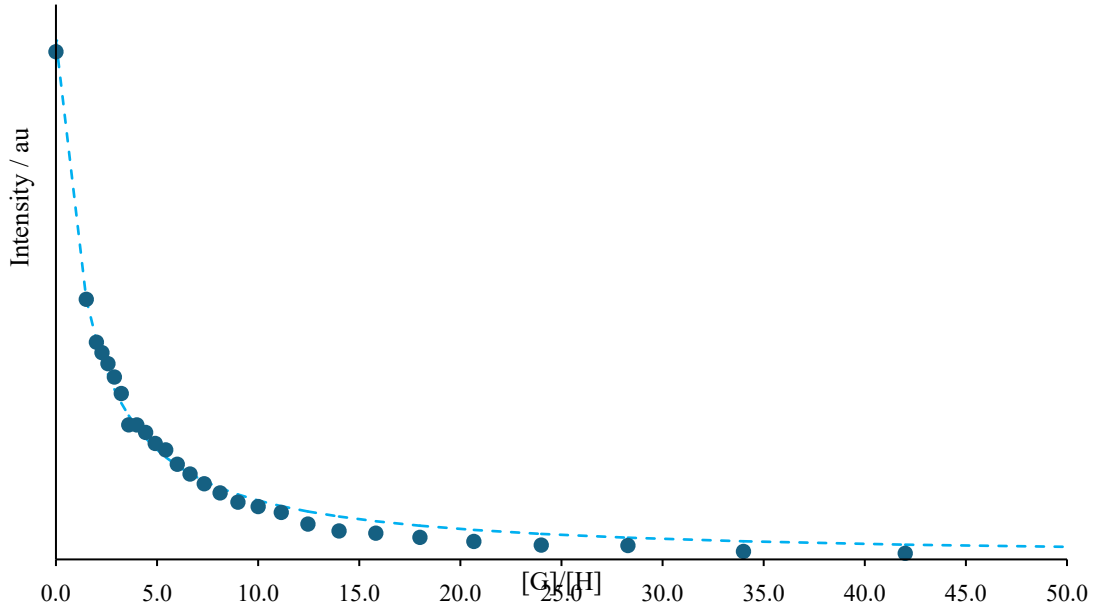

Fig. S20: Luminescence spectroscopic titration involving addition of portions of **Co_8** to SRB (10 μM) in phosphate buffer (0.1 M, pH 7.0): fitting to a 1:1 binding isotherm afforded the association constant K_b = 6.7 x 10^4 M^{-1}.

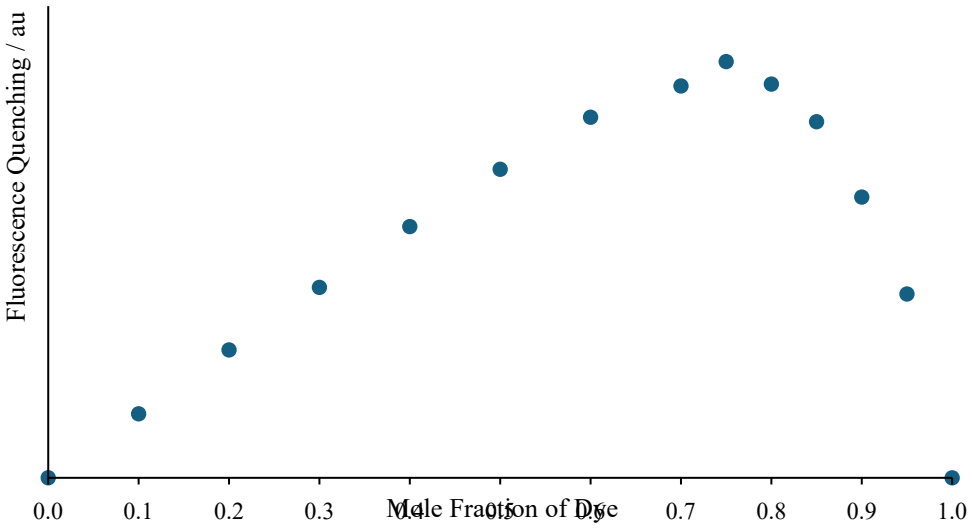

Fig. S21: Job plot showing degree of fluorescence quenching for varying **Co_8**/**FLU** mole fractions at a total concentration of 10 μM in phosphate buffer (0.1 M, pH 7.0), indicating *ca.* 3:1 **FLU:Co_8** binding at this concentration.

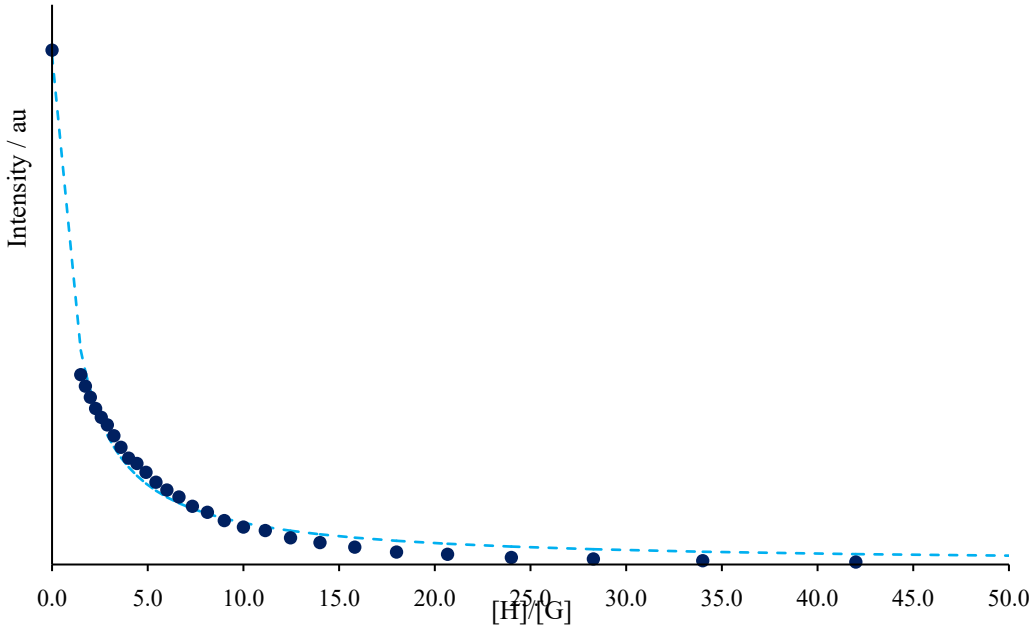

Fig. S22: Fluorescence spectroscopic titration of **FLU** and **Co_8** (10 μM) in phosphate buffer (0.1 M, pH 7.0): fitting to a 1:1 binding isotherm afforded the association constant (K_b = 1.2 x 10^5 M^{-1}).

S3 – Dye Degradation Studies

UV/vis measurements to follow the the dye degradation reactions were recorded using an Implen Nanophotometer C40 spectrophotometer.

Stock solutions of each complex [**M_1** (M = Fe, Co, Ni, Zn); **Co_4**; **M_8** (M = Fe, Co, Ni, Zn); **Co_{12}**] were prepared by stirring roughly 10 mg in TWEEN20 (200 µL) followed by addition of phosphate buffer (2 mL, 0.1 M, pH 7.0) and further stirring for 2 hours then filtration to remove any undissolved solid. The concentration of each solution was then determined by UV/vis spectroscopy; solutions were subsequently diluted with buffer to the desired concentration (**M_1**: 450 µM, **Co_4**: 112.5 µM, **M_8**: 56.25 µM, **Co_{12}** 37.5 µM). Stock solutions of the dyes **FLU**, **CFLU**, **EY**, **RB** and **SRB** (375 µM) were made using the same buffer and concentrations determined by UV/vis spectroscopy. Peroxymonosulfate (PMS) stock solutions (17 mM) were made by dissolving $KHSO_5$ (25.8 mg, 0.17 mmol) in water (10 cm^3). PMS solutions were prepared fresh each day and kept in low light conditions to minimise spontaneous activation.

The dye degradation reactions were followed by UV/vis measurements of the intensity of the dye absorption maximum (**FLU**, 489 nm; **CFLU**, 490 nm; **EY**, 511 nm; **RB**, 552 nm; **SRB**, 563 nm) over 30 mins with measurements at intervals of 5 seconds. Dye stock solution (20 µL), cage stock solution (10 µL) and buffer (950 µL) were combined and agitated vigorously using a vortex generator. The reaction was then initiated by addition of the PMS stock solution (20 µL) rapidly followed by vigorous agitation (<1 s) and measurement of the first UV/vis absorption datapoint. Each experiment was performed at least twice, and the UV/Vis spectra were checked at the end of catalytic runs to confirm cage integrity.

Below are shown example normalised individual reaction profiles for degradation of **CFLU** and **EY**, with and without **Co_8** present as a catalyst, from which the first-order rate constants in Table 1 (main text) are derived using analysis of initial rates. All five catalysed reaction curves are collected in Fig. 8 (main text).

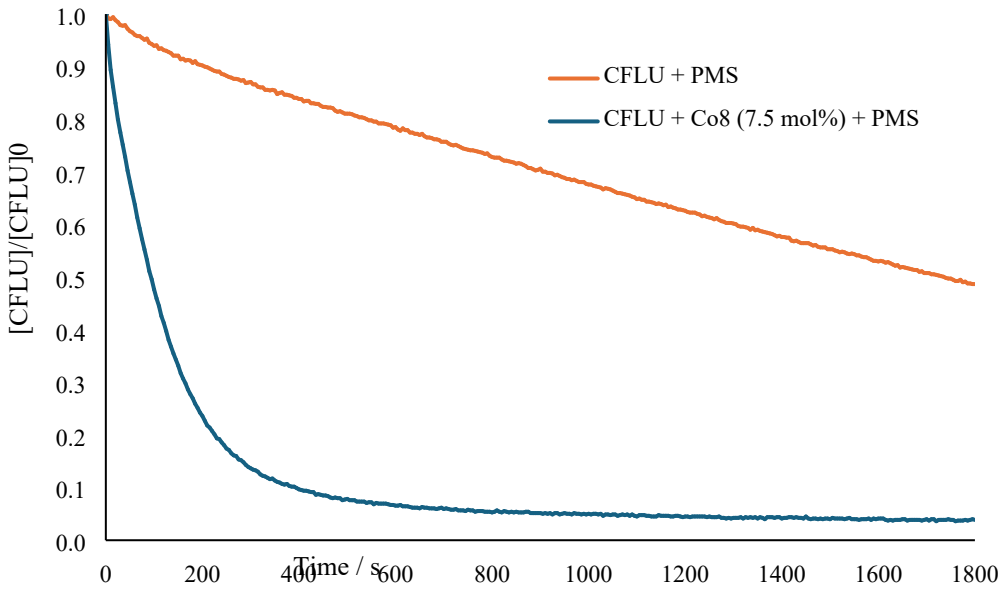

Fig. S23: Normalised UV-vis absorption intensity at λ = A_{max} over time, for the uncatalyzed (orange line) and for **Co_8**-catalysed (blue line) and degradation of **CFLU** (7.5 µM) by PMS (45 eq.) in phosphate buffer (0.1 M, pH 7.0).

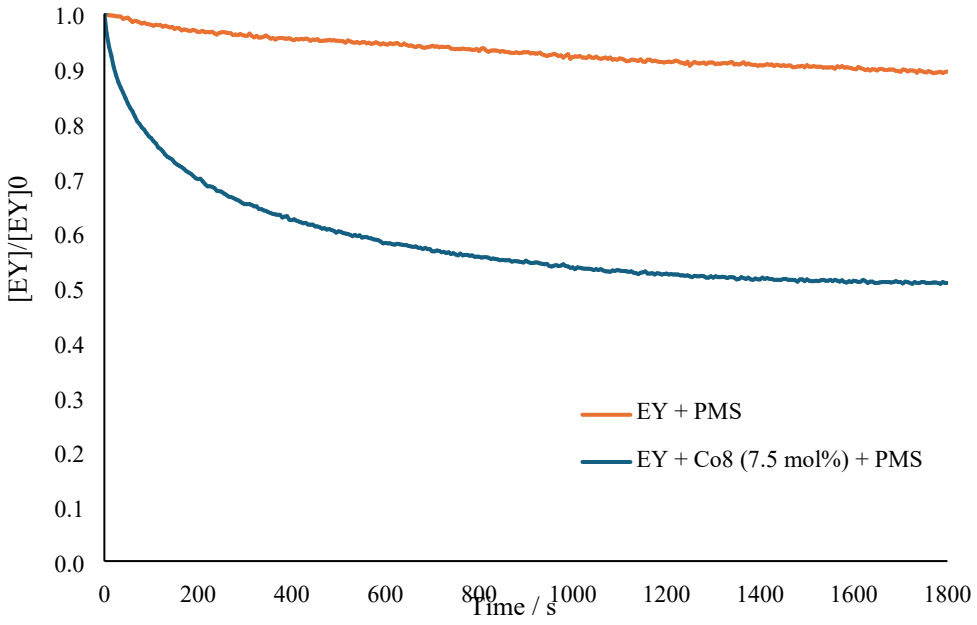

Fig. S24: Normalised UV-vis absorption intensity at λ = A_{max} over time, for the uncatalyzed (orange line) **Co_8**-catalysed (blue line) and degradation of **EY** (7.5 μM) by PMS (45 eq.) in phosphate buffer (0.1 M, pH 7.0).

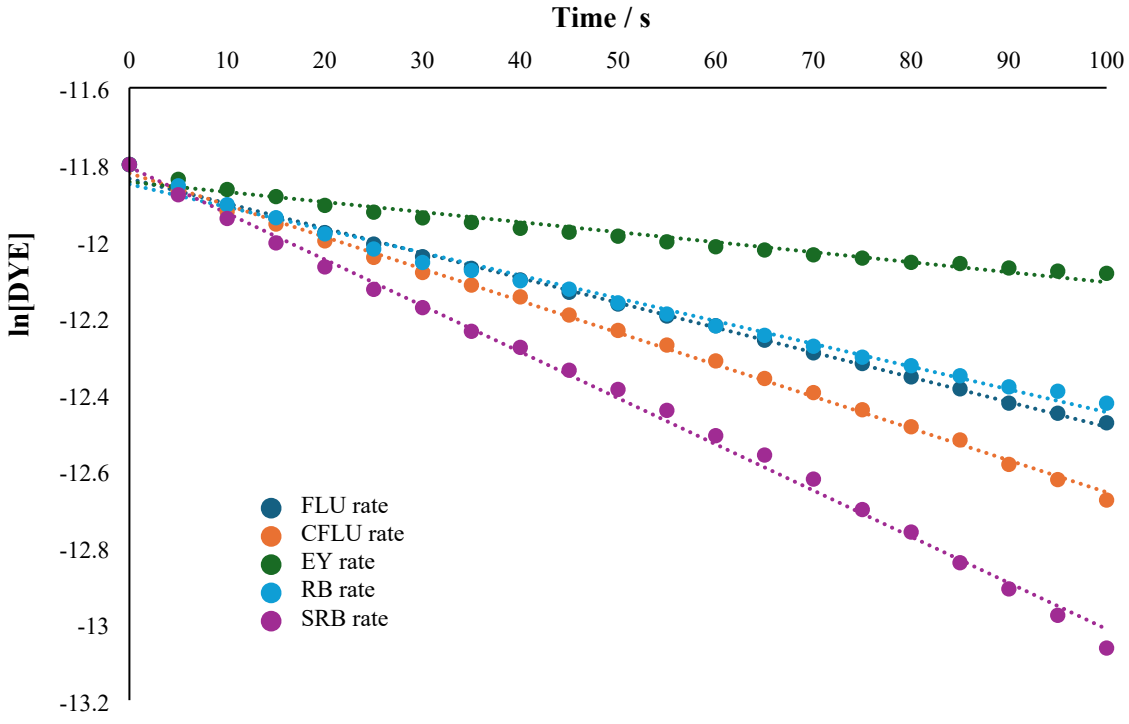

Fig. S25: Natural log of dye (**FLU, CFLU, EY, RB, SRB**) concentration over time showing first order kinetic behaviour in initial stages of the dye degradation by PMS catalysed by **Co_8** (see reaction progress curves in Fig. 8 of main text). Gradients of the fitted lines were used to calculate the initial rate constants which are included in Table 1, lines 3 and 5 – 8.

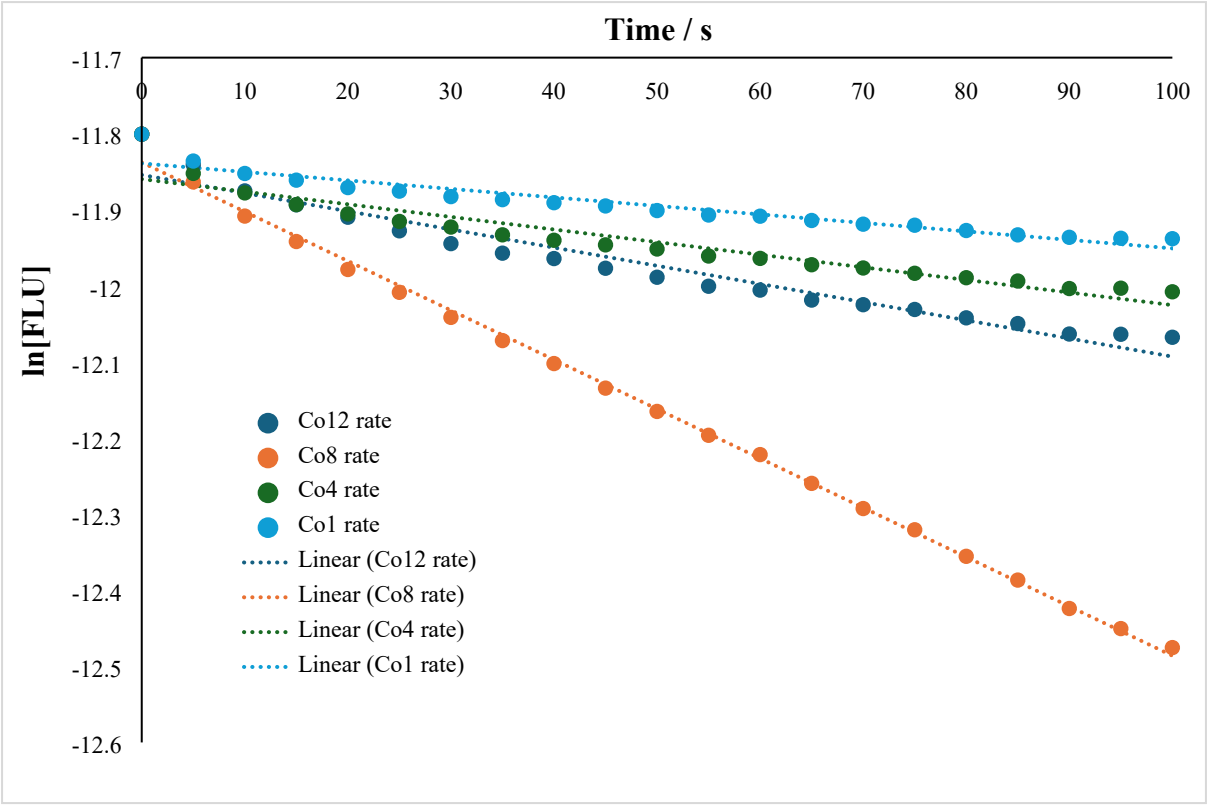

Fig. S26: Natural log of **FLU** dye concentration over time showing first order kinetic behaviour in initial stages of the dye degradation by PMS catalysed by $\mathbf{Co_1}$, $\mathbf{Co_4}$, $\mathbf{Co_8}$ and $\mathbf{Co_{12}}$ (see reaction progress curves in Fig. 7 of main text). Gradients of the fitted lines were used to calculate the initial rate constants which are included in Table 1, lines 1 – 4.

S4 – X-ray crystallography

Details of the crystal used, data collection and refinement parameters are given in Table S1 (below). Diffraction data were collected on a Rigaku / Oxford Diffraction Synergy S instrument equipped with a HyPix-6000HE Hybrid Photon Counting (HPC) detector. The data were integrated and an absorption correction applied using the CrysAlisPro software.[S1] The structures were solved with Olex2,[S2] using dual space iterative methods (SHELXT)[S3] and refined by a full-matrix least-squares algorithm (SHELXL).[S3] As usual in structures of this type (refs. 2 – 4, main text), disorder of anions and solvent molecules which could not be successfully modelled necessitated use of a solvent mask function to remove diffuse electron density; and weak scattering necessitated extensive use of geometric and displacement parameter restraints, to provide a stable refinement and a physically reasonable model. Full details are in the CIFs.

Table S1. Crystal parameters, data collection and refinement details for the crystal structures[a]

Complex	**Ni_8•EY**	**Ni_8•SRB**	**Fe_8**	**Co_1**
CCDC number	2455100	2455101	2455103	2455102
Formula	$C_{401}H_{398.2}B_{10.45}Br_{6.8}Cl_{0.15}F_{41.88}N_{72}Ni_8O_{40}$	$C_{406.5}H_{427.5}B_{10.82}F_{43.28}N_{75}Ni_8O_{40.5}S_3$	$C_{372.2}H_{412.8}B_{12.75}Cl_{1.55}F_{51}Fe_8N_{72}O_{38.2}$	$C_{27}H_{27}B_2CoF_8N_9$
Molecular weight	8791.64	8516.85	8114.69	710.12
Crystal system	triclinic	triclinic	Monoclinic	monoclinic
Space group	*P*–1	*P*–1	*C*2/c	$P2_1/n$
a/Å	21.8986(4)	21.4417(2)	32.9811(2)	12.6814(4)
b/Å	22.3981(4)	22.1353(2)	30.0048(2)	12.1894(4)
c/Å	43.4906(8)	24.3064(3)	39.7967(3)	20.2334(8)
α/°	104.597(2)	78.5620(10)	–	90
β/°	98.324(2)	72.3190(10)	96.4540(10)	104.141(4)
γ/°	94.218(2)	88.9640(10)	–	90
V/Å^3	20290.2(7)	10762.1(2)	39132.9(5)	3032.88(19)
Z	2	1	4	4
ρ/g cm^{-3}	1.439	1.314	1.377	1.555
Crystal size/mm^3	0.21 x 0.05 x 0.03	0.50 x 0.10 x 0.10	0.06 x 0.06 x 0.06	0.04 x 0.02 x 0.01
μ/mm^{-1}	1.986	1.274	3.244	5.205
Data, restraints, parameters	78392, 1206, 4837	44489, 551, 2495	38176, 722, 2388	5984, 496, 569
R_{int}, R_{sigma}	0.1465, 0.1141	0.0788, 0.0369	0.0436, 0.0371	0.0392, 0.0359
Final R_1, wR_2[b]	0.0885, 0.2636	0.0949, 0.3252	0.0698, 0.2089	0.0813, 0.2477
Largest peak/hole/e Å^{-3}	2.15, –0.68	1.70, –0.91	1.55, –0.82	1.10, –0.61

[a] Conditions in common to all structures: Cu-Kα radiation (wavelength 1.54184 Å), T = 100K

[b] The value of R_1 is based on 'observed' data with $I > 2\sigma(I)$; the value of wR_2 is based on all data.

References

S1 CrysAlisPro Software system (version 1.171.40.45a), Rigaku Oxford Diffraction, UK, **2018**.

S2 O. V. Dolomanov, L. J. Bourhis, R. J. Gildea, J. A. K. Howard, H. Puschmann, *J. Appl. Cryst.* **2009**, *42*, 339.

S3 G. M. Sheldrick, *Acta Crystallogr. Sect. A* **2015**, *71*, 3.